Sci Model Simul (2008) 15:97–121
DOI 10.1007/s10820-008-9109-x

Atomistic simulation studies of complex carbon and silicon systems using environment-dependent tight-binding potentials

Cai-Zhuang Wang · Gun-Do Lee · Ju Li · Sidney Yip · Kai-Ming Ho

Published online: 19 November 2008
© Springer Science+Business Media B.V. 2008

1 Introduction

The use of tight-binding formalism to parametrize electronic structures of crystals and molecules has been a subject of continuous interests since the pioneer work of Slater and Koster [1] more than a half of a century ago. Tight-binding method has attracted more and more attention in the last 20 years due to the development of tight-binding potential models that can provide interatomic forces for molecular dynamics simulations of materials [2–7]. The simplicity of the tight-binding description of electronic structures makes the method very economical for large-scale electronic calculations and atomistic simulations [5,9]. However, studies of complex systems require that the tight-binding parameters be "transferable", [4] i.e., to be able to describe accurately the electronic structures and total energies of a material in different bonding environments. Although tight-binding molecular dynamics has been successfully applied to a number of interesting systems such as carbon fullerenes and carbon nanotubes, [10,11] the transferability of tight-binding potentials is still the major obstruction hindering the wide spread application of the method to more materials of current interest.

There are two major approximations made in a typical tight-binding representation of effective one-electron Hamiltonian matrix or band structure based on the Slater-Koster theory

C.-Z. Wang (✉) · K.-M. Ho
Ames Laboratory-U.S. DOE and Department of Physics and Astronomy, Iowa State University, Ames, IA 50011, USA
e-mail: wangcz@ameslab.gov

G.-D. Lee
School of Materials Science and Engineering and Inter-university Semiconductor Research Center (ISRC), Seoul National University, Seoul 151-742, Korea

J. Li
Department of Materials Science and Engineering, University of Pennsylvania, Philadelphia, PA 19104, USA

S. Yip
Department of Nuclear Science and Engineering and Department of Materials Science and Engineering, Massachusetts Institute of Technology, Cambridge, MA 02139, USA

[1]. One is the use of a fixed minimal basis set, i.e., the basis orbitals for a given atom type are not allowed to vary according to structures or bonding environments, and another is the two-center approximation which assumes that the crystal potential can be constructed as a sum of spherical potentials centered on atoms, and contribution from atom k's spherical potential on matrix element between two basis orbitals on atoms i and j can be neglected. Experiences from the tight-binding parametrizations have indicated that the transferability of tight-binding models are limited by both approximations [7,12–14].

Several attempts to go beyond the above two approximations have been shown to improve the transferability of the tight-binding descriptions of electronic structures and total energies [12–14]. For example, Mehl and Papaconstantopoulos found that by incorporating a crystal-field like term into the tight-binding model and allowing the on-site atomic energies to vary according to the bonds surrounding of the atoms have significant improvement on the accuracy and transferability of the tight-binding models to describe metallic systems [12]. Wang et al. introduced an environment-dependent tight-binding model that allows the tight-binding parameters to vary not only with the interatomic distances but also according to the bonding environment around the interacting pair of atoms, and showed that the environment-dependent tight-binding model describes well not only the properties of the lower-coordinated covalent but also those of higher-coordinated metallic structures of carbon and silicon [13,14].

In this article, we will review some progress on tight-binding modeling and simulations based on the environment-dependent tight-binding model. In particular, application of the EDTB potentials to the studies of complex systems such as vacancy diffusion and reconstruction in grapheme, dislocation climb and junction formation in carbon nanotubes, addimer diffusion on Si surfaces as well as grain boundary and dislocation core structures of in silicon will be discussed in more details.

2 Environment-dependent tight-binding potential model

2.1 General formalism of tight-binding potential model

The expression for the binding energy (or potential energy) of a system in a tight-binding molecular dynamics simulation is given by

$$E_{\text{binding}} = E_{\text{bs}} + E_{\text{rep}} - E_0 \tag{1}$$

The first term on the right hand side of Eq. (1) is the band structure energy which is equal to the sum of the one-electron eigenvalues ε_i of the occupied states given by a tight-binding Hamiltonian H_{TB} which will be specified later,

$$E_{\text{bs}} = \sum_i f_i \varepsilon_i \tag{2}$$

where f_i is the electron occupation (Fermi-Dirac) function and $\sum_i f_i = N_{\text{electron}}$.

The second term on the right hand side of Eq. (1) is a repulsive energy and can be expressed as a functional of sum of short-ranged pairwise interactions,

$$E_{\text{rep}} = \sum_i f\left(\sum_j \phi\left(r_{ij}\right)\right) \tag{3}$$

where ϕ_{ij} is a pairwise repulsive potential between atoms i and j, and f is a function which for example can be a 4th order polynomial [15] with argument $x = \sum_j \phi\left(r_{ij}\right)$,

$$f(x) = \sum_{n=0}^{4} c_n x^n \tag{4}$$

If $f(x) = x/2$, the repulsive energy is just a simple sum of pairwise potential $\phi\left(r_{ij}\right)$. In our environment-dependent tight-binding (EDTB) potential model that will be discuss in the following, we adopt the expression of Eq. (4) for the repulsive energy E_{rep}.

The term E_0 in Eq.(1) is a constant which represents the sum of the energies of the individual atoms. In our model, E_0 is absorbed into E_{bs} and E_{rep} respectively so that E_0 is set to be zero.

The tight-binding Hamiltonians H_{TB} for the electronic structure calculation is expressed as

$$H_{\mathrm{TB}} = \sum_i \sum_{\alpha=s,p} e_{i\alpha} a_{i\alpha}^{+} a_{i\alpha} + \sum_{i,j} \sum_{\alpha,\beta=s,p} h_{i\alpha,j\beta} a_{i\alpha}^{+} a_{j\beta} \tag{5}$$

where $e_{i\alpha}$ is the on-site energy of the α orbital on site i, $a_{i\alpha}^{+}$ and $a_{i\alpha}$ are the creation and annihilation operators, respectively. $h_{i\alpha,j\beta}$ is the hopping integral between α and β orbitals located at sites i and j, respectively. For a system described by only s and p orbitals, there are four types of hopping integrals $h_{ss\sigma}$, $h_{sp\sigma}$, $h_{pp\sigma}$, and $h_{pp\pi}$. In general, the Hamiltonian matrix elements between the orbitals on sites i and j should be dependent on the vector $\mathbf{R_j} - \mathbf{R_i}$. as well as the atomic configuration around these sites. However, under the two-center approximation made by Slater and Koster [1], the integrals are dependent only on the separation distance of the two atoms and can be parameterized by fitting to *ab initio* band structures. Once the hopping integrals are obtained, the TB Hamiltonian matrix can be constructed by linear combination of the hopping integrals using the direction cosines of the vector $\left(\mathbf{R_j} - \mathbf{R_i}\right)$ [1]

2.2 EDTB potential model formalism

In our EDTB potential model for carbon and silicon [13,14], the minimal basis set of sp^3 orbitals is taken to be orthogonal. The tight-binding Hamiltonian H_{TB} takes the form as in the Slater-Koster theory discussed above, but the effects of orthogonalization, three-center interactions and the variation of the local basis set with environment are taken into account empirically by renormalizing the interaction strength between atom pairs according to the surrounding atomic configurations. The TB hopping parameters and the repulsive interaction between atoms i and j depend on the environments of atoms i and j through two scaling functions. The first one is a screening function that is designed to weaken the interactions between two atoms when there are intervening atoms between them. Another is a bond-length scaling function which scales the interatomic distance (hence the interaction strength) between the two atoms according to their effective coordination numbers. Longer effective bond lengths are assumed for higher coordinated atoms.

Specifically, the hopping parameters and the pairwise repulsive potential as the function of atomic configurations are expressed as

$$h\left(r_{ij}\right) = \alpha_1 R_{ij}^{-\alpha_2} \exp\left(-\alpha_3 R_{ij}^{\alpha_4}\right)\left(1 - S_{ij}\right) \tag{6}$$

In Eq. (6), $h\left(r_{ij}\right)$ denotes the possible types of interatomic hopping parameters $h_{ss\sigma}, h_{sp\sigma}, h_{pp\sigma}, h_{pp\pi}$ and pairwise repulsive potential $\phi\left(r_{ij}\right)$ between atoms i and j. r_{ij} is the real distance and R_{ij} is a scaled distance between atoms i and j. S_{ij} is a screening function. The parameters $\alpha_1, \alpha_2, \alpha_3, \alpha_4$, and parameters for the bond-length scaling function R_{ij} and the screening function S_{ij} can be different for different hopping parameters and the pairwise repulsive potential. Note that expression Eq. (6) reduces to the traditional two-center form if we set $R_{ij} = r_{ij}$ and $S_{ij} = 0$.

The screening function S_{ij} is expressed as a hyperbolic tangent (tanh) function (i.e., $S_{ij} = \tanh\left(\xi_{ij}\right)$

$$S_{ij} = \frac{\exp\left(\xi_{ij}\right) - \exp\left(-\xi_{ij}\right)}{\exp\left(\xi_{ij}\right) + \exp\left(-\xi_{ij}\right)} \tag{7}$$

with argument ξ_{ij} given by

$$\xi_{ij} = \beta_1 \sum_l \exp\left[-\beta_2\left(\frac{r_{il} + r_{jl}}{r_{ij}}\right)^{\beta_3}\right] \tag{8}$$

where β_1, β_2, and β_3 are adjustable parameters. Maximum screening effect occurs when atom l is situated close to the line connecting atoms i and j (i.e., $r_{il} + r_{jl}$ is a minimum). This approach allows us to distinguish between first and further neighbor interactions without explicit specification. This is well-suited for molecular dynamics simulations where it is difficult to define exactly which atoms are first-nearest neighbors and which are second-nearest neighbors.

The bond-length scaling function R_{ij} scales the interatomic distance between two atoms according to their effective coordination numbers. Longer effective bond lengths are assumed for higher coordinated atom pairs therefore interaction strength in larger-coordinated structures is reduced. The scaling between the real and effective interatomic distance is given by

$$R_{ij} = r_{ij}\left(1 + \delta_1\Delta + \delta_2\Delta^2 + \delta_3\Delta^3\right) \tag{9}$$

where $\Delta = \frac{1}{2}\left(\frac{n_i - n_0}{n_0} + \frac{n_j - n_0}{n_0}\right)$ is the fractional coordination number relative to the coordination number (n_0) of the diamond structure, averaged between atoms i and j. The coordination number can be modeled by a smooth function,

$$n_i = \sum_j \left(1 - S_{ij}\right) \tag{10}$$

with a proper choice of parameters for S_{ij} which has the form of the screening function described above (Eq. (7)). The parameters for the coordination number calculations in carbon and silicon will be given in next subsections, respectively.

Besides the hopping parameters, the diagonal matrix elements are also dependent on the bonding environments. The expression for the diagonal matrix elements is

$$e_{\lambda,i} = e_{\lambda,0} + \sum_j \Delta e_\lambda\left(r_{ij}\right) \tag{11}$$

where $\Delta e_\lambda\left(r_{ij}\right)$ takes the same expression as Eq. (6), λ denotes the two types of orbitals (s or p). $e_{s,0}$ and $e_{p,0}$ are the on site energies of a free atom.

Finally, the repulsive energy term is expressed in a functional of the sum of pairwise interactions as defined in Eq. (4) in the previous section.

To ensure that all interactions go to zero smoothly at the given cutoff distance $r_{\rm cut}$, all the distance dependent parameters in the model are multiplied by an attenuation function of the form of $\cos^2\theta$ with

$$\theta = \frac{\pi}{2}\frac{r - r_{\rm match}}{r_{\rm cut} - r_{\rm match}} \tag{12}$$

when the distance is $r_{\rm match} < r < r_{\rm cut}$. This attenuation function can guarantee that the distance dependent parameters and their first derivatives are continuous at $r_{\rm match}$ and go to zero at $r_{\rm cut}$.

3 EDTB potential for carbon and its applicationa

3.1 EDTB potential for carbon

Carbon is a strong covalently bonded material best described by the tight-binding scheme. In 1996, Tang, Wang, Chan, and Ho developed an environment-dependent tight-binding potential for carbon following the formalism described in the previous subsection [13]. The parameters of this potential are given in Tables 1 and 2. In addition to the parameters listed in the tables, the parameters for calculating the coordination number of carbon using Eq. (10) are $\beta_1 = 2.0$, $\beta_2 = 0.0478$, $\beta_3 = 7.16$. The cutoff distance for the interaction is $\mathrm{r_{cut}} = 3.4$Å and $\mathrm{r_{match}} = 3.1$Å (see Eq. (12). As shown in Fig. 1, the environment-dependent tight-binding potential model for carbon describes very well the binding energies not only for the covalent (diamond, graphite, and linear chain) structures, but also for the higher-coordinated metallic (bcc, fcc, and simple cubic) structures, as compared to the two-center tight-binding model developed by us earlier [15]. The EDTB potential is also more accurate for elastic constants and phonon frequencies of diamond and graphite structures as compare to the two-center tight-binding model (Tables 3, 4).

Table 1 The parameters of the EDTB model for carbon

	α_1	α_2	α_3	α_4	β_1	β_2	β_3	δ
$h_{ss\sigma}$	−8.9491	0.8910	0.1580	2.7008	2.0200	0.2274	4.7940	0.0310
$h_{sp\sigma}$	8.3183	0.6170	0.1654	2.4692	1.0300	0.2274	4.7940	0.0310
$h_{pp\sigma}$	11.7955	0.7620	0.1624	2.3509	1.0400	0.2274	4.7940	0.0310
$h_{pp\pi}$	−5.4860	1.2785	0.1383	3.4490	0.2000	8.500	4.3800	0.0310
ϕ	30.0000	3.4905	0.00423	6.1270	1.5035	0.205325	4.1625	0.002168
$\Delta e_s, \Delta e_p$	0.1995275	0.029681	0.19667	2.2423	0.055034	0.10143	3.09355	0.272375

The TB hopping integrals are in the unit of eV and the interatomic distances are in the unit of Å. ϕ is dimensionless

Table 2 The coefficients (in unit of eV) of the polynomial function $f(x)$ for the EDTB potential for carbon

c_0	c_1	c_2	c_3	c_4
12.201499972	0.583770664	$0.336418901 \times 10^{-3}$	$-0.5334093735 \times 10^{-4}$	$0.7650717197 \times 10^{-6}$

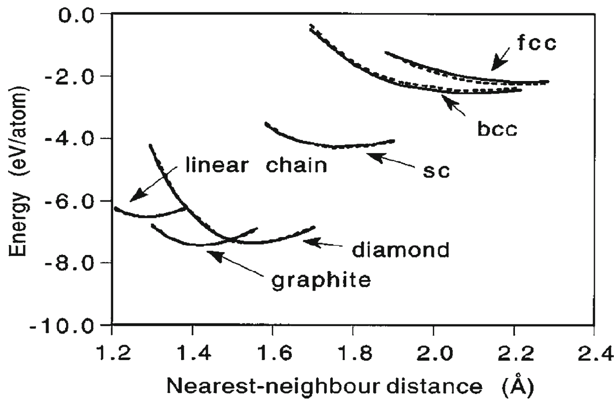

Fig. 1 Cohesive energies as a function of nearest neighbor distance for carbon in different crystalline structures calculated using the environment-dependent TB model are compared with the results from the first-principles DFT-GGA calculations. The solid curves are the TB results and the dashed curves are the GGA results (From Ref. [13])

Table 3 Elastic constants, phonon frequencies and Grünneisen parameters of diamond calculated from the XWCH-TB model [15] and the environment-dependent TB (EDTB) model [13] are compared with experimental results [16]

	XWCH	EDTB	Experiment
a(Å)	3.555	3.585	3.567
B	4.56	4.19	4.42
c_{11}–c_{12}	6.22	9.25	9.51
c_{44}	4.75	5.55	5.76
$\upsilon_{LTO}(\Gamma)$	37.80	41.61	39.90
$\upsilon_{TA}(X)$	22.42	25.73	24.20
$\upsilon_{TO}(X)$	33.75	32.60	32.0
$\upsilon_{LA}(X)$	34.75	36.16	35.5
$\gamma_{LTO}(\Gamma)$	1.03	0.93	0.96
$\gamma_{TA}(X)$	−0.16	0.30	
$\gamma_{TO}(X)$	1.10	1.50	
$\gamma_{LA}(X)$	0.62	0.98	

Elastic constants are in units of 10^{12}dyn/cm^2 and the phonon frequencies are in terahertz

Table 4 Elastic constants, phonon frequencies and Grüneisen parameters of graphite calculated from the XWCH-TB model [15] and the environment-dependent TB (EDTB) model [13] are compared with experimental results [17,18]

	XWCH	EDTB	Experiment
c_{11}–c_{12}	8.40	8.94	8.80
E_{2g2}	49.92	48.99	47.46
A_{2u}	29.19	26.07	26.04
$\gamma(E_{2g2})$	2.00	1.73	1.63
$\gamma(A_{2u})$	0.10	0.05	

Elastic constants are in units of 10^{12}dyn/cm^2 and the phonon frequencies are in terahertz

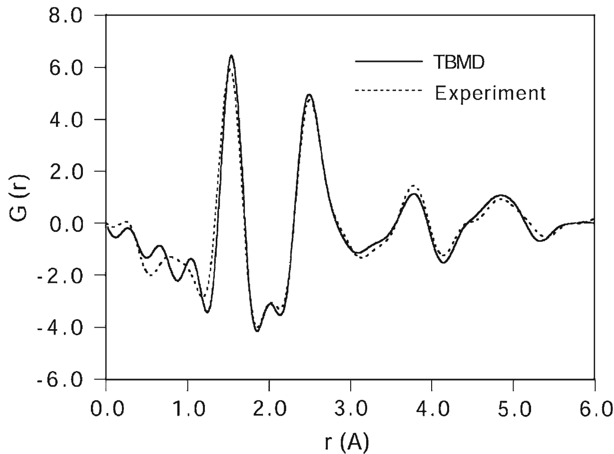

Fig. 2 Radial distribution functions G(r) of the tetrahedral amorphous carbon structure generated by tight-binding molecular dynamics using the environment-dependent TB potential (solid curve) are compared with the neutron scattering data of Ref. [22] (dotted curve). The theoretical result has been convoluted with the experimental resolution corresponding to the termination of the Fourier transform at the experimental maximum scattering vector $Q_{max} = 16\,Å^{-1}$. (From Ref. [25])

Another example that demonstrates the better transferability of the EDTB model over the two-center model for complex simulations is the study of diamond-like amorphous carbon. Diamond-like (or tetrahedral) amorphous carbon consists of mostly sp^3 bonded carbon atom produced under highly compressive stress which promotes the formation of sp^3 bonds, in contrast to the formation of sp^2 graphite-like bonds under normal conditions [19–22]. Although the two-center XWCH carbon potential can produce the essential topology for the diamond-like amorphous carbon network [23], the comparison with experiment is not quite satisfactory as one can see from Fig. 2. There are also some discrepancies in ring statistics between the two-center potential generated and *ab initio* molecular dynamics generated diamond-like amorphous carbon model [24]. Specifically, a small fraction of 3 and 4-membered rings observed in the *ab initio* model is absent from the results of the two-center tight-binding model. These subtle deficiencies are corrected when the EDTB potential is used to generate diamond-like amorphous carbon [25,26]. The radial distribution function of the diamond-like a-c obtained from the EDTB potential is in much better agreement with experiment as one can see from Fig. 2.

3.2 TBMD simulation of vacancy diffusion and reconstruction in grapheme

Recently, the EDTB carbon potential by Tang et al. [13] has been further improved by Lee et al. by incorporating an angle dependence factor into the repulsive energy to describe correctly the diffusion of an adatom and a vacancy in carbon nanotubes and graphene [27–30]. The modified EDTB carbon potential has described successfully the reconstruction of vacancy defects in a graphene and carbon nanotubes [27–30].

Vacancy defects in graphene layers, which are usually generated by ion or electron irradiations of graphite or carbon nanotubes, have been an interesting subject of many studies, yet the dynamics and reconstruction of the defects in graphene layer are still not well understood [31–35]. Figure 3 illustrates the snapshots of the atomic processes of diffusion, coalescence,

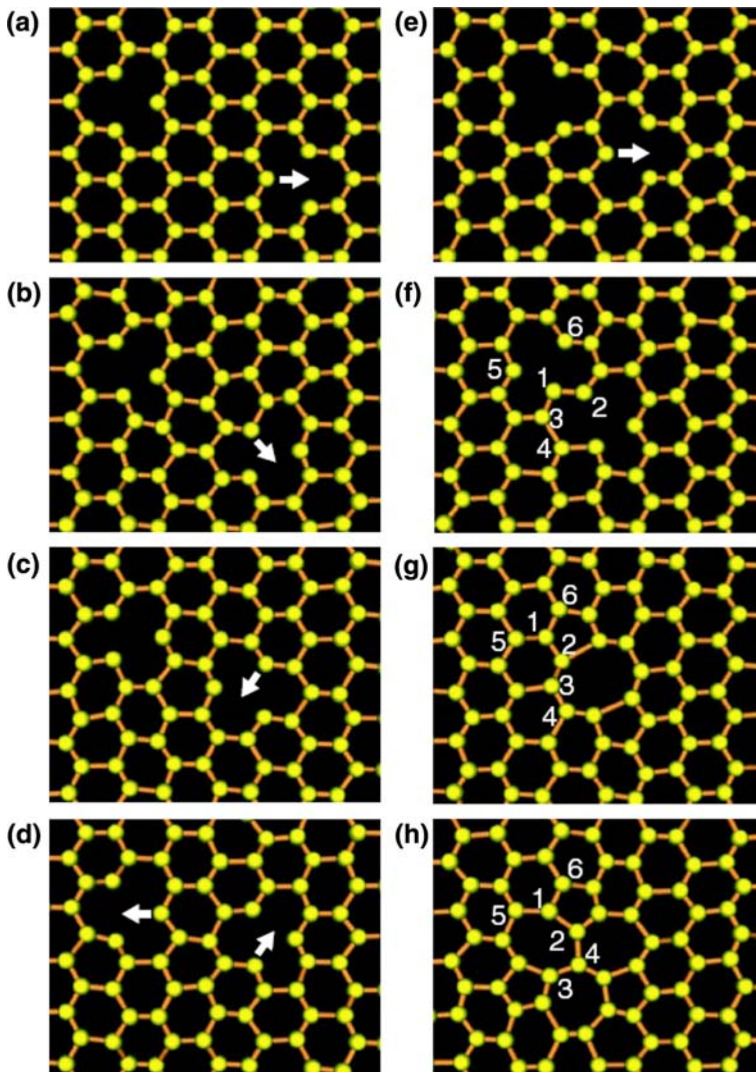

Fig. 3 Atomic processes from the TBMD simulations for vacancy diffusion in a graphene layer. (**a**) 0 K (at time $t = 0$ ps), (**b**) ~3000 K ($t = 2.7$ ps), (**c**) ~3000 K ($t = 3.0$ ps), (**d**) ~2900 K ($t = 3.3$ ps), (**e**) ~3000 K ($t = 5.0$ ps), (**f**) ~3100 K ($t = 6.0$ ps), (**g**) ~3100 K ($t = 6.5$ ps), and (**h**) ~3800 K ($t = 125$ ps). White arrows indicate the direction for the carbon atom to jump in the next step. The atoms involved in the diffusion process are labeled with the numbers. (From Ref. [27])

and reconstruction of vacancy defects in graphene layers during the simulation using molecular dynamics with the improved EDTB carbon potential. The TBMD simulations in Fig. 3 shows that two single vacancies diffuse and coalesce into a 5-8-5 double vacancy at the temperature of 3000 K, and it is further reconstructed into a new defect structure, the 555–777 defect, by the Stone-Wales type transformation at higher temperatures. The stability of the defect structures observed in the TBMD simulations is further examined by first-principles calculations which show that the graphene layer containing the 555–777 defect, as shown

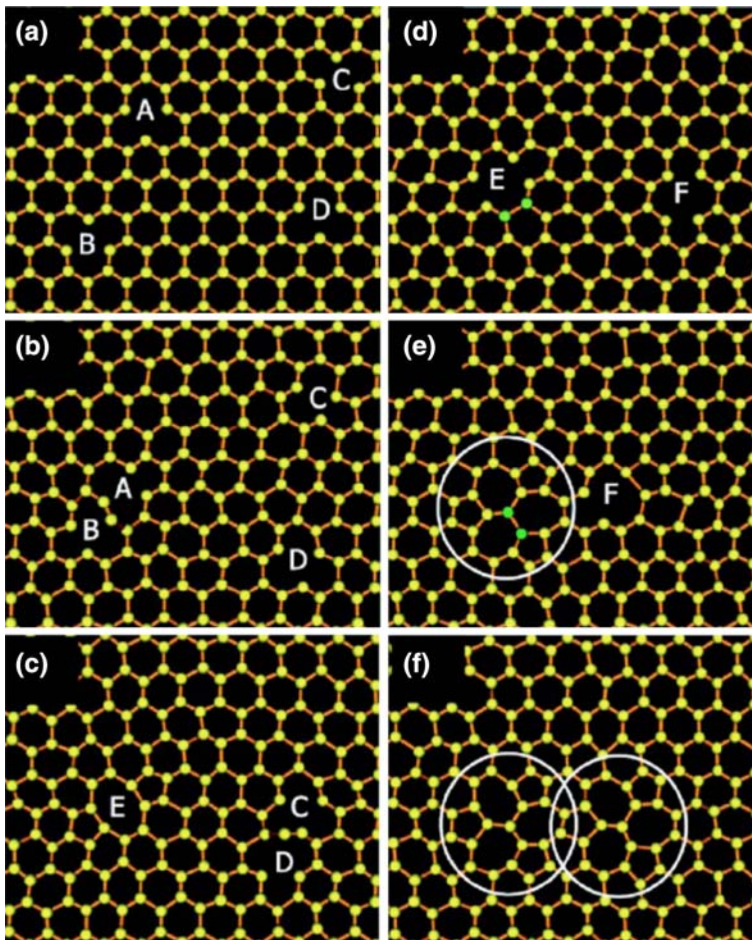

Fig. 4 Atomic processes from the TBMD simulations of four vacancy defects in a graphene layer. (**a**) 0 K (at time $t = 0$ ps); (**b**) ∼3000 K ($t = 5.5$ ps); (**c**) ∼3000 K ($t = 52.6$ ps); (**d**) ∼3900 K ($t = 86.8$ ps); (**e**) ∼3700 K ($t = 274.4$ ps); (**f**) ∼3700 K ($t = 281.6$ ps)

in Fig. 3h, is most stable and its formation energy is lower than that of the 5-8-5 defect by 0.91 eV. The formation energy of the two separated single vacancies (Fig. 3a) is much higher than that of the 555–777 defect by 8.85 eV.

The simulations are also performed for four single vacancies in a graphene sheet. As shown in Fig. 4 the four single vacancies in the graphene layer first coalesce into two double vacancies, each consists of a pentagon-heptagon-pentagon (5-8-5) defective structure. While one of the 5-8-5 defects further reconstructs into a 555–777 defect, which is composed of three pentagonal rings and three heptagonal rings, the another 5-8-5 defect diffuses toward to the reconstructed 555–777 defect. During the 5-8-5 defect diffusion process, three interesting mechanisms, i.e., "dimer diffusion", "chain diffusion", and "single atom diffusion", are observed. Finally, the four single vacancies reconstruct into two adjacent 555–777 defects, forming a local haeckelite structure proposed by Terrones et al. [36].

3.3 TBMD simulation of junction formation in carbon nanotubes

The improved EDTB carbon potential has also been applied in tight-binding molecular dynamics simulation to study the junction formation through self-healing of vacancies, in single-walled carbon nanotubes (SWCNT) [29,30]. Figure 5 shows the atomic details of vacancy reconstruction in a (16,0) SWCNT with a six-vacancy hole by the TBMD simulation [29,30]. The TBMD simulation is performed starting from a relaxed six-vacancy hole geometry as shown in Fig. 5a. In the early stage of the simulation, the SWCNT is heated up to high temperature through a constant-temperature molecular dynamics simulation. It was found that rearrangement of carbon atoms around the vacancy hole starts to occur near 4500 K at the simulation time of 18 ps through the rotation of carbon dimers, i.e., Stone-Wales transformation. After 19 ps of the simulation time, three hexagons at the lower left corner of the vacancy hole (those containing the atoms 1-4 in Fig. 5b) are recombined into a pentagon-octagon-pentagon defect by successive Stone-Wales transformations of the dimers 1-2 and 3-4 as shown in Fig. 5b. After the simulation time of 20 ps, another two hexagons (containing the atoms 5-7) on the other side of the vacancy hole are also reconstructed into one pentagon and one heptagon by the Stone-Wales transformation of the dimer 5-6. In order to prevent the evaporation of carbon atoms, the system is then cooled down to 3,000 K for 4 ps and the vacancy hole is healed during this simulation period as shown in Fig. 5c. The structure immediately after the healing process consists of four pentagons and four heptagons with a two-fold rotation symmetry. The pentagon a and b and the heptagon c and d are related to the pentagon e and f and the heptagon g and h, respectively through the 2-fold axis which goes through the center of the carbon bond between atom 2 and 6. After the simulation time of 24 ps, the system is heated up again to 4,500 K for 7 ps and another structural reconstruction among the defects is observed. As shown in Fig. 5c and d, as the result of a Stone-Wales transformation of the dimer 1-3, the two heptagons (c and d in Fig. 5c) and one pentagon (b in Fig. 5c) on the left side of the 2-fold symmetry axis are transformed into three hexagons while one hexagonal ring containing the carbon atom 3 is transformed into a heptagonal ring. Finally a pentagon-heptagon pair defect, which has been observed in the experiment after the irradiation [37], is emerged through the reconstruction process. Since the dimer 5-7 is equivalent to the dimer 1-3 due to the 2-fold symmetry at the stage of Fig. 5c, the dimer 5-7 is expected to undergo a similar Stone-Wales transformation. Indeed, after 41 ps of simulation time, the Stone-Wales transformation happens to the carbon dimer 5-7. Consequently another pentagon-heptagon pair defect is formed at the right side of the 2-fold axis in the same way as the formation of the previous pentagon-heptagon pair on the left side of the 2-fold axis. The structure with two pentagon-heptagon pairs in Fig. 5e is very stable energetically and can sustain its shape without any changes for more than 20 ps in the simulation even at a temperature $\sim$4,500 K. At the final stage of the simulation, the system is gradually cooled down to 0 K in 12.5 ps and the structure with two pentagon-heptagon pair defects is found to maintain without any additional reconstruction as shown in Fig. 5f.

Because each pentagon-heptagon is a topological dislocation defect of the grapheme sheet, Fig. 5 in fact shows an elementary dislocation climb process. Unlike dislocation glide [38,39] which conserves the number of atoms while relaxing stress, dislocation climb is a non-conservative process that requires removal or addition of atoms by radiation knock-out, vacancy diffusion, evaporation, etc. Fig. 5 is akin to the collapse of a vacancy disk and the formation of Frank edge dislocation loop in metals [40]. We expect that once the edge dislocation dipole (two pentagon-heptagon of opposite polarity) is formed, as shown in Fig. 5, further mass removal and chirality change can occur in a steady fashion by a pentagon-heptagon defect moving up the tube axial direction. Dislocation climb is also stress-coupled,

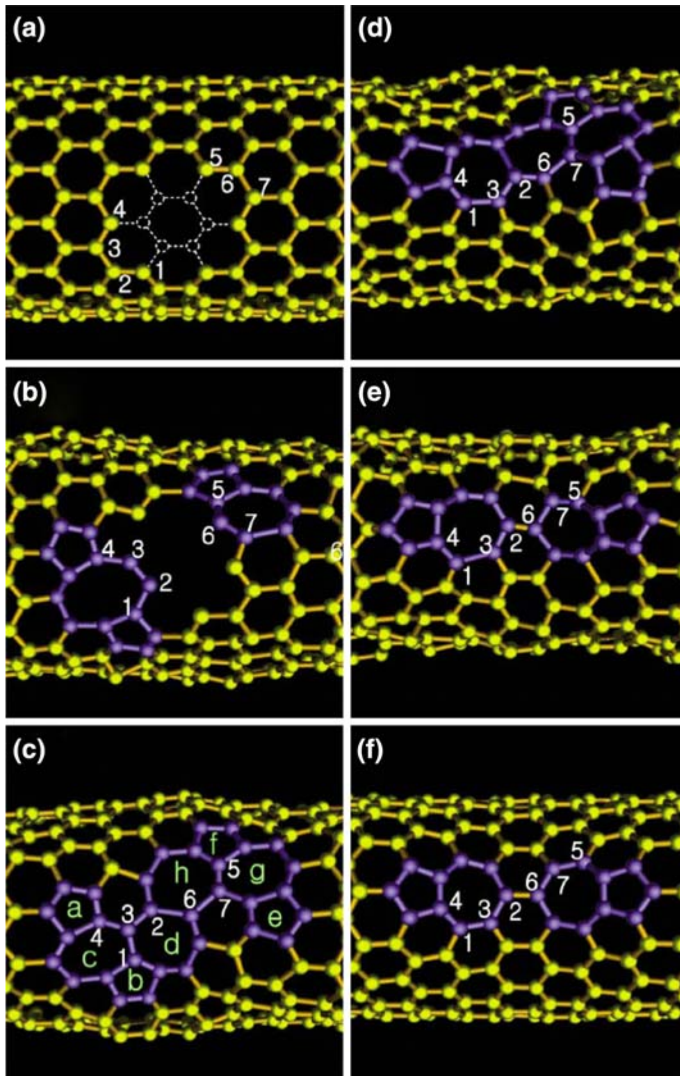

Fig. 5 Atomic processes from the TBMD simulations of a (16, 0) SWCNT with six vacancies. (**a**) 0 K (at time t = 0 ps); (**b**) ~4,500 K (t ≈ 20.2 ps); (**c**) ~3,100 K (t ≈ 23.2 ps); (**d**) ~4,400 K (t ≈ 32.3 ps); (**e**) ~4,700 K (t ≈ 41.5 ps); (**f**) ~90 K (t ≈ 53.9 ps). The carbon atoms on the rear side of the tube are concealed in figures in order to see the reconstruction of vacancies more clearly. Dotted circles in (A) indicate the positions of the six carbon vacancies in the perfect (16, 0) SWCNT. Yellow colors indicate carbon atoms and bonds in hexagonal rings. Blue colors indicate carbon atoms and bonds in non-hexagonal rings. See the text for small letters in (C) and numbers. (From Ref. [29])

which means tensile force on the nanotube can aid/impede climbing motion of the pentagon-heptagon and mass removal/addition, which may shift the semiconductor-metal junctions at high temperatures.

Figure 6 shows the front view of the initial and final structure from the TBMD simulation. The vacancy hole in the initial structure is healed up in the final structure and the radius of the tube in the middle section is reduced. The diameter and chirality in the center

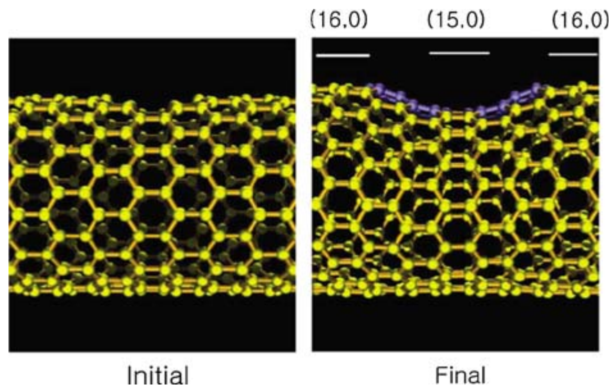

Fig. 6 Front views of initial and final structure from TBMD simulation for (16, 0) SWCNT with six vacancies. The initial structure corresponds to Fig. 5a. The final structure corresponds to Fig. 1f. (From Ref. [29])

part of the final structure is found to be (15, 0), which is one of the metallic SWCNTs. In order to understand the effects of the vacancy cluster size on the formation of junctions, they have also performed the TBMD simulation to study the junction formation dynamics of a (16, 0) SWCNT containing a hole of ten vacancies. The formation of two pentagon-heptagon pair defects is also observed, with the mechanism similar to that in the simulation of the (16, 0) SWCNT with six vacancies discussed earlier in this subsection. The most interesting difference between the simulation results of the ten and six vacancies is that the length of the (15, 0) tube section is longer with ten vacancies. These simulation results demonstrate that intramolecular semiconductor-metal junctions of SWCNTs can be produced by irradiation followed by a proper annealing which allow various vacancy defects generated by the irradiation to reconstruct into the pentagon-heptagon pairs at the junction. These simulations also suggest a mechanism for synthesis of carbon nanotube semiconductor-metal intramolecular junctions with specific locations and controlled sizes and show the possibility of application to nanoelectronic devices.

4 EDTB potential for silicon and its applications

4.1 EDTB potential for silicon

Although the diamond structure of Si also exhibits covalent sp^3 bonding configurations, the higher coordinated metastable structures of Si are metallic and with energies close to that of the diamond structure. Therefore, Si can be metallic under high pressures or at high temperatures. For example, the coordination of the liquid phase of Si is close to the coordination of the metallic structures (i.e., 6.5). These properties of Si pose a challenge for accurate tight-binding modeling of Si: it is difficult to describe the low-coordinated covalent structures and high-coordinated metallic structures with good accuracy using one set of tight-binding parameters. With the environment-dependent tight-binding formalism, Wang, Pan, and Ho show that this difficulty can be overcome [14]. The EDTB Si potential developed by them gives excellent fit to the energy vs interatomic distance of various silicon crystalline structures with different coordination as shown in Fig. 7. The EDTB Si potential also describes well the structure and energies of Si surfaces in addition to other bulk properties such as elastic constants and phonon frequencies [14]. These results can be seen from Tables 5 and 6. The parameters of the EDTB Si potential are listed in Tables 7 and 8. The parameters for calculating

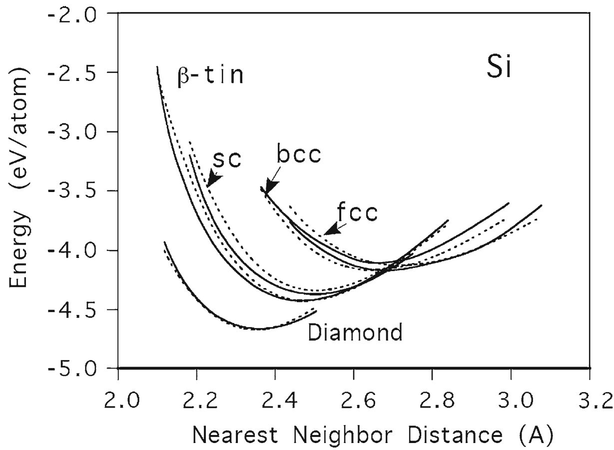

Fig. 7 cohesive energies as a function of nearest neighbor distance for silicon in different crystalline structures calculated using the environment-dependent TB model are compared with the results from the first-principles DFT-LDA calculations. The solid curves are the TB results and the dashed curves are the LDA results. (From Ref. [14])

the coordination number of Si using the Eq. (10) are $\beta_1 = 2.0$, $\beta_2 = 0.02895$, $\beta_3 = 7.96284$. The cutoff distances for the interaction are $r_{cut} = 5.2$ Å and $r_{match} = 4.8$ Å (see Eq. (12)).

A useful benchmark for Si interatomic potentials is a series of model structures for the $\Sigma = 13\{510\}$ symmetric tilt boundary structures in Si [41]. Eight different structures as indicated in the horizontal axis of Fig. 8 have been selected for the calculations. These structures were not included in the database for fitting the parameters. The structures are relaxed by steepest-decent method until the forces on each atom were less than 0.01 eV/Å. The energies obtained from the calculations using the EDTB Si potential are compared with the results from *ab initio* calculations, and from two-center Si tight-binding potentials [42], and classical potential calculations [43,44] as shown in Fig. 8. The energy differences for different structures predicted by the EDTB calculations agree very well with those from the *ab initio* calculations. The energies from the two-center tight-binding potentials and classical potentials do not give the correct results in comparison with the results from *ab initio* and environment tight-binding potential calculations even though the atoms in the structures are all four-fold coordinated.

4.2 TBMD simulation studies of addimer diffusion on Si(100) surface

The EDTB silicon potential has been used to investigate the diffusion pathways and energy barriers for Si addimer diffusion along the trough and from the trough to the top of dimer row on Si(100) surface [45,46]. Diffusion of Si addimers on the Si(100) surface have attracted numerous experimental and theoretical investigations [47–52] because it plays an essential role in the homoepitaxial growth of silicon films.

Clean Si(100) surfaces exhibit a $c(4 \times 2)$ reconstruction in which the surface Si atoms form a row of alternating buckled dimers along the [010] direction [53,54]. There are four principal addimer configurations [47,51] on the Si(100) as shown in Fig. 9. An addimer can sit on top of a dimer row (A and B) or in the trough between two rows (C and D), with its axis oriented either parallel (A and D) or perpendicular (B and C) to the dimer-row direction. All four

Table 5 The parameters obtained from the fitting for the EDTB model of Si [14]. The α_1 is in the unit of eV. Other parameters are dimensionless

	α_1	α_2	α_3	α_4	β_1	β_2	β_3	δ_1	δ_2	δ_3
$h_{ss\sigma}$	−5.9974	0.4612	0.1040	2.3000	4.4864	0.1213	6.0817	0.0891	0.0494	−0.0252
$h_{sp\sigma}$	3.4834	0.0082	0.1146	1.8042	2.4750	0.1213	6.0817	0.1735	0.0494	−0.0252
$h_{pp\sigma}$	11.1023	0.7984	0.1800	1.4500	1.1360	0.1213	6.0817	0.0609	0.0494	−0.0252
$h_{pp\pi}$	−3.6014	1.3400	0.0500	2.2220	0.1000	0.1213	6.0817	0.4671	0.0494	−0.0252
ϕ	126.640	5.3600	0.7641	0.4536	37.00	0.56995	19.30	0.082661	−0.023572	0.006036
$\Delta e_s, \Delta e_p$	0.2830	0.1601	0.050686	2.1293	7.3076	0.07967	7.1364	0.7338	−0.03953	−0.062172

Table 6 The coefficients of the polynomial function $f(x)$ for the EDTB potential of Si

	$c_0\ (eV)$	c_1	$c_2\ \left(eV^{-1}\right)$	$c_3\ \left(eV^{-2}\right)$	$c_4\ \left(eV^{-3}\right)$
$x \geq 0.7$	-0.739×10^{-6}	0.96411	0.68061	−0.20893	0.02183
$x < 0.7$	−1.8664	6.3841	−3.3888	0.0	0.0

Table 7 Elastic constants and phonon frequencies of silicon in the diamond structure calculated from the two-center TB model [42] and the environment-dependent TB (EDTB) model [14] are compared with experimental results [16]

	Two-center TB	EDTB	Experiment
a(Å)		5.450	5.430
B	0.876	0.90	0.978
c_{11}–c_{12}	0.939	0.993	1.012
c_{44}	0.890	0.716	0.796
$\upsilon_{LTO}(\Gamma)$	21.50	16.20	15.53
$\upsilon_{TA}(X)$	5.59	5.00	4.49
$\upsilon_{TO}(X)$	20.04	12.80	13.90
$\upsilon_{LA}(X)$	14.08	11.50	12.32

Elastic constants are in units of 10^{12}dyn/cm^2 and the phonon frequencies are in terahertz

Table 8 Surface energies of the silicon (100) and (111) surfaces from the EDTB Si potential [14]

Structure	Surface energy	ΔE
Si(100)		
(1 × 1)-ideal	2.292	0.0
(2 × 1)	1.153	−1.139
p(2 × 2)	1.143	−1.149
c(4 × 2)	1.148	−1.144
Si(111)		
(1 × 1)-ideal	1.458	0.0
(1 × 1)-relaxed	1.435	−0.025
(1 × 1)-faulted	1.495	0.037
$\sqrt{3} \times \sqrt{3} - t_4$	1.213	−0.245
$\sqrt{3} \times \sqrt{3} - h_3$	1.346	−0.112
(2 × 1)-Haneman	1.188	−0.270
(2 × 1)-π-bonded chain	1.138	−0.320
(7 × 7)-DAS	1.099	−0.359

ΔE is the energy relative to that of the (1 × 1)-ideal surface. The energies are in the unit of eV/(1 × 1)

configurations have been identified in scanning tunneling microscopy (STM) experiments [55]. Addimer configuration A is the lowest energy configuration. The relative energies of the four addimer configurations A, B, C, and D are 0.0, 0.02, 0.28, and 1.02 eV respectively from the tight-binding calculations as compare to 0.0, 0.03, 0.24, and 0.91 eV respectively from first principles calculations.

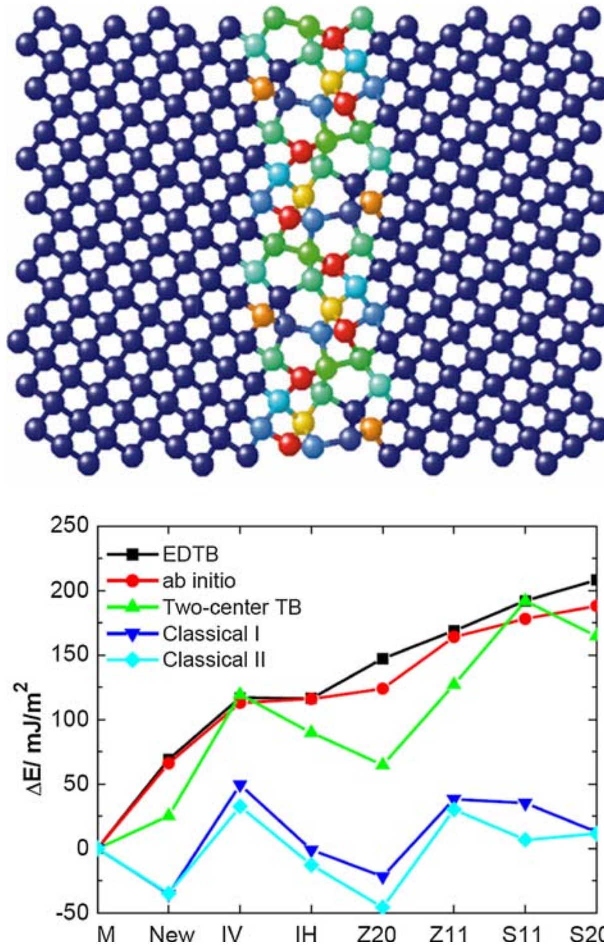

Fig. 8 Energies of the $\Sigma = 13\{510\}$ symmetric tilt boundary structures in Si. Eight different structures as indicated in the horizontal axis were selected for calculations. The energies are relative to that of the structure M which has been identified by experiment. The energies obtained from the calculations using the EDTB Si potential are compared with results from *ab initio* calculations, and from two-center Si tight-binding potentials [42], and classical potential calculations (classical I [43] and classical II [44]). The results of EDTB, *ab initio*, and classical I are taken from Ref. [41]

Experimental evidence and theoretical calculations [49,52] suggest that the diffusion of addimers has an anisotropic property: they prefer diffusion along the top of the dimer rows. However, using the atom tracking method [56], addimer diffusion along the troughs as well as crossing the trough to the next dimer row at a temperature of 450 K, in addition to the diffusion along the top of the dimer rows has also been observed [57]. The energy barrier for addimer to diffuse along the trough and to leave the trough to the top of the dimer row are estimated by STM experiment to be 1.21 ± 0.09 eV and 1.36 ± 0.06 eV respectively [57].

Because the unit cell used in such calculations contains a large number of atoms, a comprehensive search for the low energy barriers diffusion pathway is very expensive using *ab initio* methods. Here we have employed tight-binding molecular dynamics calculations to explore the possible diffusion pathways and select plausible candidate pathways for study by

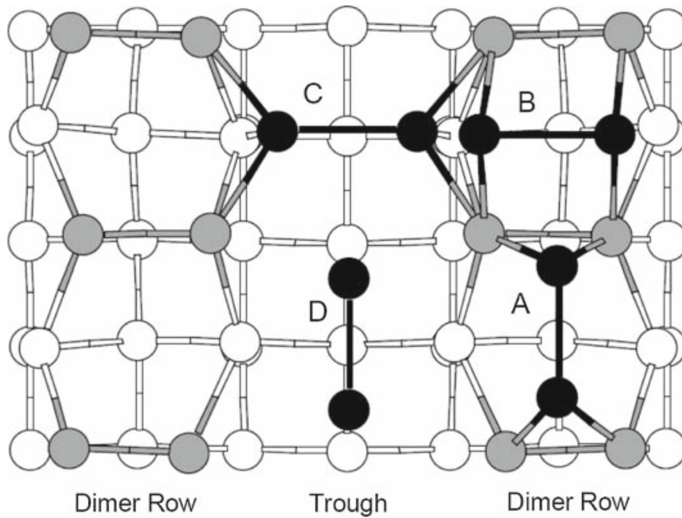

Fig. 9 Schematic drawing of the four principal dimer configurations on Si(100). Black circles represent the Si addimers, the gray circles represent the dimer atoms of the Si(100) substrate, and the open circles represent the subsurface atoms

more accurate *ab initio* calculations. The tight-binding studies reveal new pathways which have diffusion barriers in excellent agreement with the experimentally estimated values. The EDTB silicon tight-binding model reproduces excellently the experimental observation and the *ab initio* calculation results for addimer diffusion and opens up the possibility of studying surface dynamics on the Si(100) surface by using tight-binding molecular dynamics.

4.2.1 Diffusion between trough and the top of dimer row

Most of the previous calculations consider a straightforward pathway for addimer diffusion from trough to the top of dimer row by a direct translational motion of perpendicular addimer from C to B (path I). The energy as the function of addimer displacement along this pathway obtained by the tight-binding calculations is plotted in Fig. 10a (solid line) which shows that the energy barrier for diffusion of an addimer from C to B along this pathway is 1.72 eV, much larger than the experimental value of 1.36 eV.

The energy barrier for the diffusion of a parallel addimer from D to A has also been investigated. The energy as a function of addimer displacement for D to A along the straight pathway is plotted in Fig. 10b (solid line). The diffusion barrier from D to A is only 0.88 eV, which is much smaller than the experimental value of 1.36 eV. However, since the energy of the D configuration is 0.74 eV higher than that of the C configuration, the total energy barrier for diffusion from C to A via D (path II) is at least 1.62 eV which is also much higher than the experimental value.

Using tight-binding molecular dynamics as a search engine, Lee el al. discovered an unusual diffusion pathway for a Si addimer to diffuse between trough and the top of the dimmer row [45]. This pathway (path III) consists of rotation of the addimer along the diffusion pathway as shown in Fig. 11. The energy along this pathway is plotted in Fig. 10c (solid line). The tight-binding calculation gives an energy barrier of 1.37 eV for addimer diffusion from C to B, in excellent agreement with the experimental value of 1.36 eV [57].

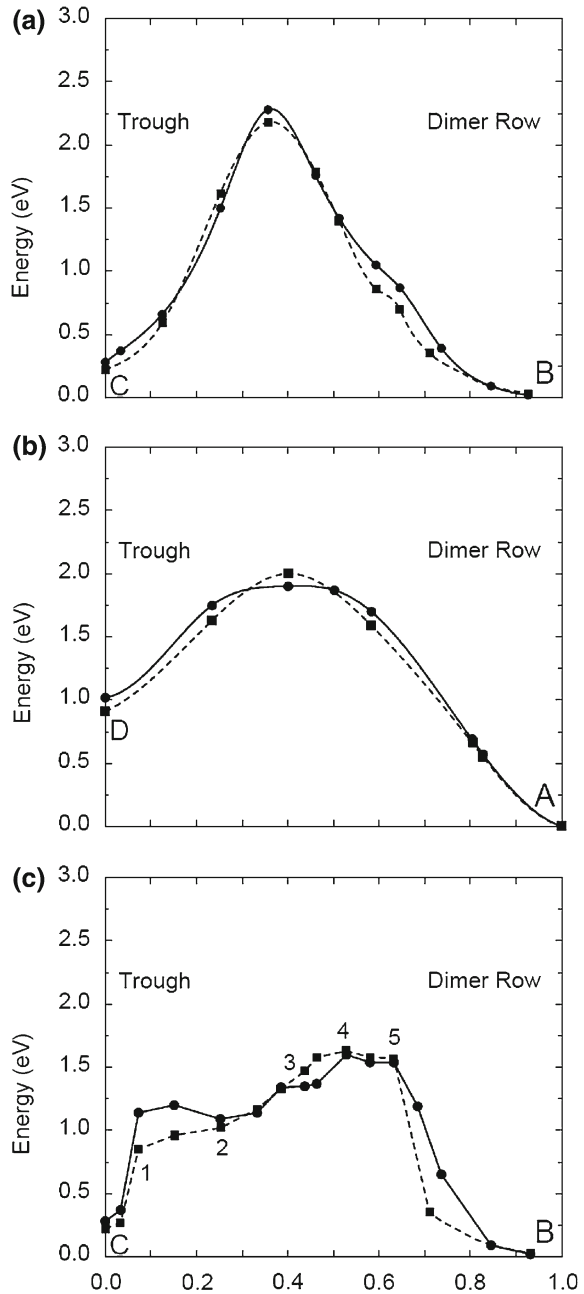

Fig. 10 The total energy variations for (**a**) the direct translational diffusion of a perpendicular addimer (path I), (**b**) the direct translational diffusion of a parallel addimer (path II), and (**c**) the diffusion consisting of rotation of addimer (path III). In each figure, solid lines represent the calculations by our tight-binding model and dashed lines represent the LDA calculations. Energies are compared with respect to the energy of the dimer configuration A in Fig. 9. The abscissa is the position of the center of the addimer from the center-line of the trough to the center-line of the dimer row. Numbers over points in figure (**c**) indicate the geometries in Fig. 11

The diffusion containing rotation is more energetically favorable than the translational diffusion of the perpendicular addimer (path I) because a smaller number of broken bonds is involved along path III.

The above results from the tight-binding calculations are further confirmed by first-principles calculations as one can see the comparison plotted in Fig. 10.

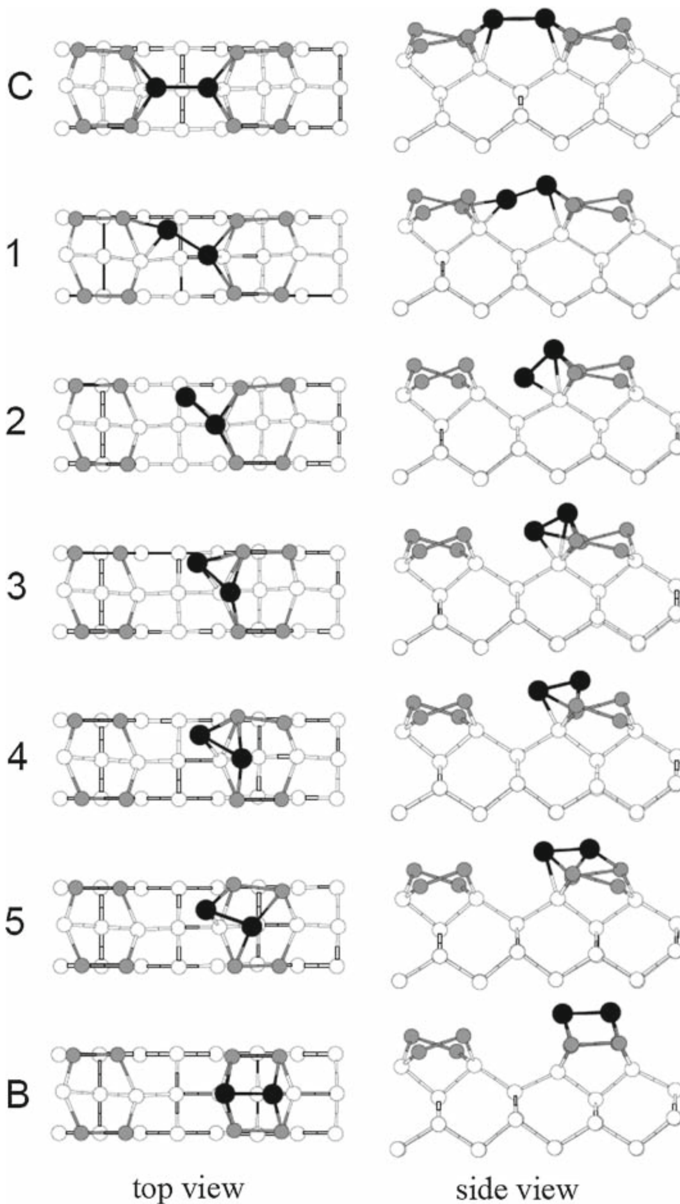

Fig. 11 Principal geometries by LDA calculations on the diffusion pathway III. Black circles represents the Si addimer, the gray circles represent the dimer atoms of the Si(100) substrate and the open circles represent the subsurface atoms. Numbering of each geometry corresponds to the number over points in Fig. 10c

4.2.2 Diffusion along the trough between the dimmer rows

Diffusion of an addimer can be viewed as a combination motion of the two individual adatoms as illustrated in top left corner of Fig. 12. The energy surface of the two silicon adatoms diffusion along the trough between the dimer rows are calculated using the environment-dependent silicon tight-binding potential. A contour plot of the resulting energy surface is

shown in Fig. 12. The ζ and ξ axes of the contour indicate the displacements of each adatom along the trough from their initial positions in geometry C, the most stable position of the addimer in the trough.

The tight-binding calculations resolve three local minima M1, M2, and M3 on the left hand side of the symmetry line PQ and two saddle points, one on the symmetry line PQ (S1) and another below the line PQ (S2). The calculations also show that addimer diffusion along the trough without dissociation or rotation (along the line C-Q-C′) has very high

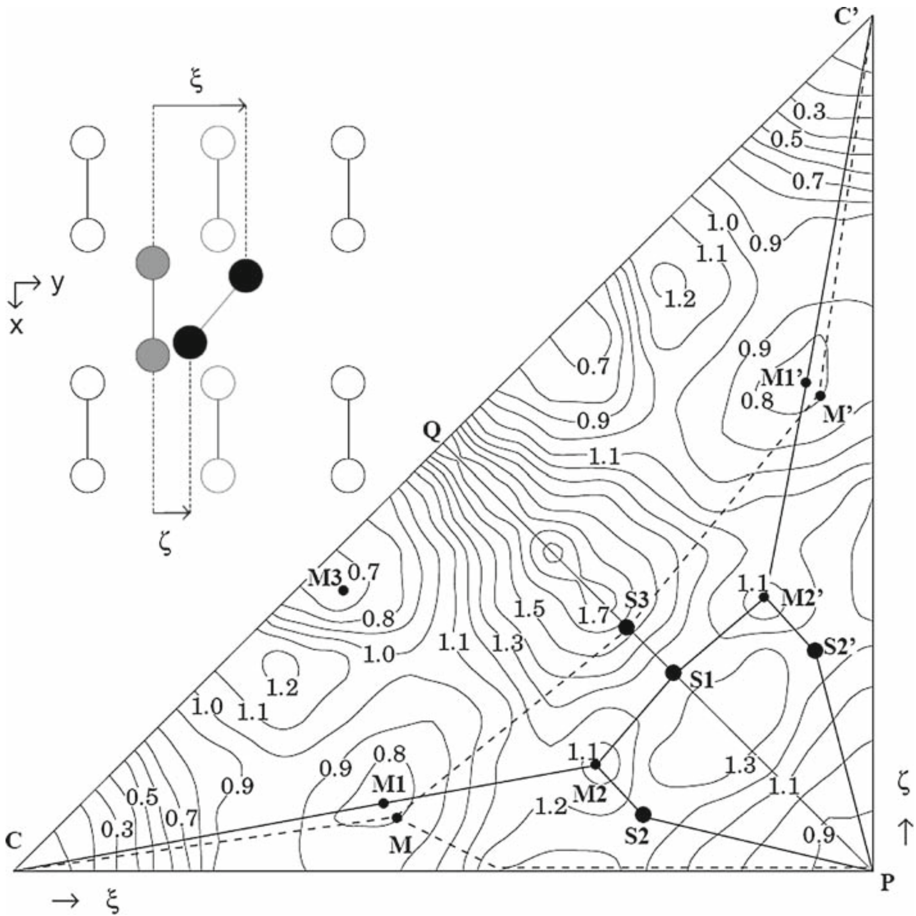

Fig. 12 The tight-binding energy contour for a dimer diffusing along the trough. Energies are in eV. The ζ and ξ axes are the displacements along the diffusion direction of the two adatoms, as illustrated in figure above (Black circles indicate the addimer, opaque circles indicate the substrate dimer atoms, and gray circles indicate the initial position of addimer). C is the initial position for the addimer, P indicates completely separated adatoms on neighboring sites, C′ indicates the addimer diffused to the neighboring site from the initial position. Line CC′ indicates the translational diffusion path without any rotation of the addimer. The line connecting Q to P indicates that the addimer on the line connecting surface dimers separates into two atoms on neighboring sites without any translation of the center of the addimer. The solid lines indicate the diffusion pathways by the tight-binding calculation. Small black spots and large black spots on the lines indicate local minima and saddle points, respectively. The dashed lines indicate the diffusion pathways by the LDA calculation. Note that the dashed lines are not related to the energy contour in this figure and are related to the position of adatoms

energy barrier of about 1.7 eV. From the resulting energy contour, one can identify two paths of diffusion which have similar low energy barriers. One path (1) follows the lines C $\rightarrow$ M1 $\rightarrow$ M2 $\rightarrow$ S2 $\rightarrow$ P $\rightarrow$ S2$'$ $\rightarrow$ M2$'$ $\rightarrow$ M1$'$ $\rightarrow$ C$'$. The other path (2) follows the lines C $\rightarrow$ M1 $\rightarrow$ M2 $\rightarrow$ S1 $\rightarrow$ M2$'$ $\rightarrow$ M1$'$ $\rightarrow$ C$'$. The local minima M1 and M2, which are surrounded by small energy barriers, are on the paths for addimer diffusion from C to C$'$. The energy barrier for path 1 is 1.26 eV. The addimer on path 1 dissociates into two monomers from M2 to P and reform at M2$'$. This pathway is similar to the dissociation pathway modeled by Goringe et al. [58]. The highest energy barrier along path 2 is 1.27 eV which is very similar to the energy barrier of path 1. However, the addimer along path 2 does not dissociate but instead rotates to minimize the energy barrier. Starting from the two best candidates for pathways predicted by the tight-binding calculations, more accurate first-principles calculations have been applied to further optimize the pathways and diffusion barriers. While the diffusion pathways after the optimization by first-principles calculations are slightly different from the tight-binding predictions, they are essentially similar and with almost identical diffusion barriers. It should be noted that without the comprehensive tight-binding calculations to search for the possible diffusion pathway, it would be very difficult for first-principles calculation to find out the correct diffusion paths and barriers for this complex system.

4.3 TBMD study of dislocation core structure in Si

The EDTB potential of Si also been applied to the study of dislocation in Si, a much more complex system. Crystalline structure of Si possess two types of (111) planes for inelastic shear, a widely separated shuffle-set (blue in Fig. 13 and a compact glide-set (red). In 2001, experiment using transmission electron microscopy (TEM) [59] show that at low temperature and high pressure, long undissociated screw dislocations appear, which cross-slip frequently. Suzuki et al. proposed [60,61] that these may be shuffle-set screw dislocations, centered at A

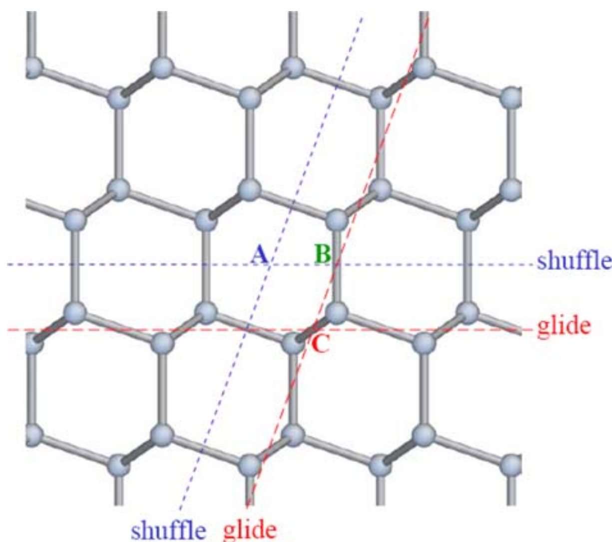

Fig. 13 Slip planes in Si, and likely centers of undissociated screw dislocations

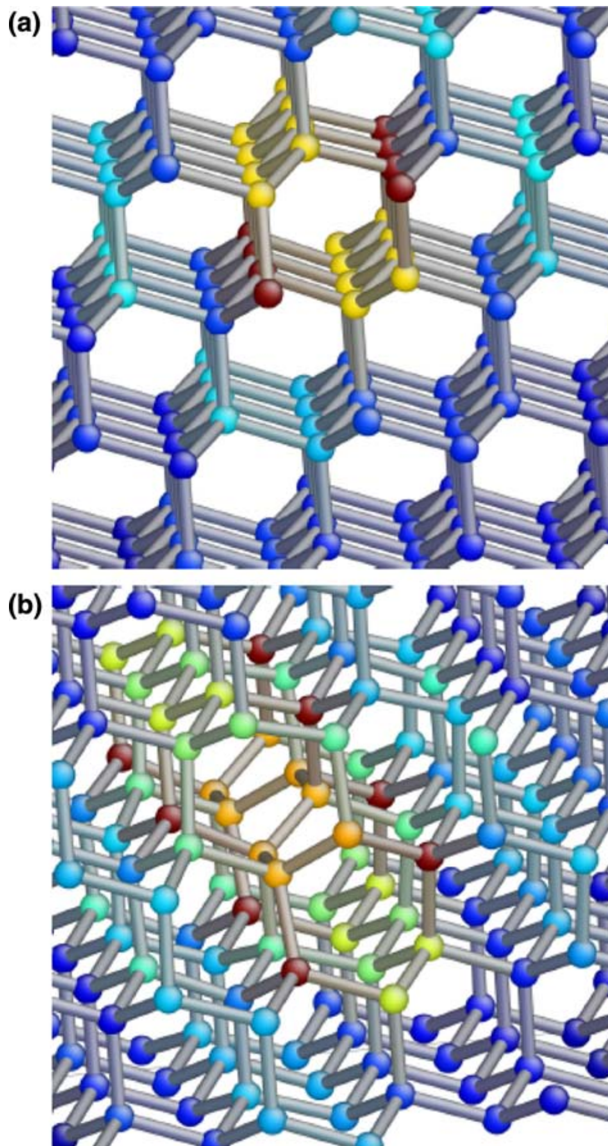

Fig. 14 (**a**) A core, and (**b**) period-doubled C core configurations. The color of atoms represents the local atomic shear strain

and B in Fig. 13 based on energy calculations using empirical classical potentials. Pizzagalli et al. then performed DFT calculations to show that the A core (Fig. 14a) has lower energy [62] than B, as well as a single-period glide-set full screw dislocation C.

Using tight-binding calculation with the EDTB silicon potential, we are able to investigate the core structure of this dislocation with larger number of atoms and with a calculation supercell that has more layers in the direction along the dislocation line [63]. We found that the C core has lower energy than A after period-doubling reconstruction in the direction along the dislocation line. This double-period C core structure is shown in Fig. 14b. Since

C can cross-slip between two glide-set planes, it satisfies all the experimental observations to date. We believe that the double-period C configuration, previously unstudied, may also play important transient roles in partial dislocation constriction and cross-slip at high temperature, and perhaps ductile-to-brittle transition [64]. The prediction from the tight-binding calculations are further confirm by first-principles calculations. We find that after the period-doubling reconstruction, the C core energy is lower than A by 0.16 eV/Å in TB, and 0.14 eV/Å in DFT. We also find that the double-period C is energetically favorable due to the electronic structure contribution. The single-period C core has a semi-metallic chain of dangling bonds which introduces electronic states near the Fermi level. This chain of dangling bonds is susceptible to Peierls distortion [65,66], leading to a period-doubling reconstruction along the chain (Fig. 14b) that opens up a wide band gap. Such an electronic mechanism is missed in the classical potential calculations.

5 Future perspective

Success of the EDTB modeling and simulations are not limited to the carbon and silicon systems as we discussed above. Its success has also been extended to the transition metal systems such as Mo [67–71], simple metal systems such as Al [72,73], and Pb [74], as well as two components systems such as Si-H [75].

In spite of these progresses, the development of environment-dependent tight-binding models so far still relies on empirical fitting to the band structure and total energies of some standard structures. The fitting procedure is quite laborious if we want to study a broad range of materials, especially in compound systems where different sets of interactions have to be determined simultaneously from a given set of electronic structures. Moreover, fundamental questions such as how and to what extent the approximations used in the Slater-Koster scheme influence the transferability of the tight-binding models are still not well understood from the empirical fitting approach. Information from first-principles calculations about these issues is highly desirable to guide the development of more accurate and transferable tight-binding models.

In general, overlap and one-electron Hamiltonian matrices from first-principles calculations cannot be used directly to infer the tight-binding parameters because fully converged first-principles calculations are done using a large basis set while tight-binding parameters are based on a minimal basis representation. Very recently, the authors and co-workers have developed a method for projecting a set of chemically deformed atomic minimal-basis-set orbitals from accurate first-principles wavefunctions [76–81]. These orbitals, referred to as "quasi-atomic minimal-basis-sets orbitals" (QUAMBOs), are highly localized on atoms and exhibit shapes close to orbitals of the isolated atom. Moreover, the QUAMBOs span exactly the same occupied subspace as the original first-principles calculation with a large basis set. Therefore, accurate tight-binding Hamiltonian and overlap matrix elements can be obtained directly from *ab initio* calculations through the construction of QUAMBOs. This new development enables us to examine the accuracy and transferability of the tight-binding models from a first-principles perspective.

Acknowledgment Ames Laboratory is operated for the U.S. Department of Energy by Iowa State University under Contract No. DE-AC02-07CH11358. This work was supported by the Director for Energy Research, Office of Basic Energy Sciences including a grant of computer time at the National Energy Research Supercomputing Center (NERSC) in Berkeley. Work of JL is supported by NSF CMMI-0728069, AFOSR, ONR N00014-05-1-0504, and Ohio Supercomputer Center.

References

1. Slater, J.C., Koster, G.F.: Phys. Rev. **94**, 1498 (1954)
2. Wang, C.Z., Chan, C.T., Ho, K.M.: Phys. Rev. B **39**, 8586 (1989)
3. Khan, F.S., Broughton, J.Q.: Phys. Rev. B **39**, 3688 (1989)
4. Goodwin, L., Skinner, A.J., Pettifor, D.G.: Europhys. Lett. **9**, 701 (1989)
5. Wang, C.Z., Chan, C.T., Ho, K.M.: Phys. Rev. B **42**, 11276 (1990)
6. Cohen, R.E., Mehl, M.J., Papaconstantopoulos, D.A.: Phys. Rev. B **50**, 14694 (1994)
7. Mercer, J.L. Jr., Chou, M.Y.: Phys. Rev. B **49**, 9366 (1993)
8. Mercer, J.L. Jr., Chou, M.Y.: Phys. Rev. B **49**, 8506 (1994)
9. Colombo, L.: In: Stauffer, D. (ed.) Annual Reviews of Computational Physics, vol. IV, p. 147. World Scientific, Singapore (1996)
10. Wang, C.Z., Chan, C.T., Ho, K.M.: Phys. Rev. Lett. **66**, 189 (1991)
11. Wang, C.Z., Chan, C.T., Ho, K.M.: Phys. Rev. B **45**, 12227 (1992)
12. Mehl, M.J., Papaconstantopoulos, D.A.: In: Fong, C.Y. (ed.) Topic in Computational Materials Science, pp. 169–213. World Scientific, Singapore (1997)
13. Tang, M.S., Wang, C.Z., Chan, C.T., Ho, K.M.: Phys. Rev. B **53**, 979 (1996)
14. Wang, C.Z., Pan, B.C., Ho, K.M.: J. Phys. Condens. Matter **11**, 2043 (1999)
15. Xu, C.H., Wang, C.Z., Chan, C.T., Ho, K.M.: J. Phys. Condens. Matter **4**, 6047 (1992)
16. Semiconductors: physics of Group IV elements and III–V compounds. In: Madelung, O., Schulz, M., Weiss, H. (eds.) Landolt-Börnstein New Series, vol. III/17a. Springer, Berlin (1982)
17. Semiconductors: intrinsic properties of Group IV elements and III–V, II–VI and I–VII Compounds. In: Madelung, O., Schulz, M. (eds.) Landolt-Börnstein New Series, vol. III/22a. Springer, Berlin (1987)
18. Dresselhaus, M.S., Dresselhaus, G.: In: Cardona, M., Guntherodt, G. (eds.) Light Scattering in Solids III, p. 8. Springer, Berlin (1982)
19. Robertson, J.: Adv. Phys. **35**, 317(1986)
20. Diamond and diamond-like films and coatings. In: Clausing R., et al. (eds.) NATO Advanced Study Institutes Series B, vol. 266, p. 331. Plenum, New York (1991)
21. McKenzie, D.R., Muller, D., Pailthorpe, B.A.: Phys. Rev. Lett. **67**, 773 (1991)
22. Gaskell, P.H., Saeed, A., Chieux, P., McKenzie, D.R.: Phys. Rev. Lett. **67**, 1286 (1991)
23. Wang, C.Z., Ho, K.M.: Phys. Rev. Lett. **71**, 1184 (1993)
24. Marks, N.A., McKenzie, D.R., Pailthorpe, B.A., Bernasconi, M., Parrinello, M.: Phys. Rev. Lett. **76**, 768 (1996)
25. Wang, C.Z., Ho K.M.: Structural trends in amorphous carbon. In: Siegal, M. P., et al. (eds.) MRS Symposium Proceedings, vol. 498 (1998)
26. Mathioudakis, C., Kopidakis, G., Kelires, P.C., Wang, C.Z., Ho, K.M.: Phys. Rev. B **70**, 125202 (2004)
27. Lee, Gun-Do, Wang, C.Z., Yoon, Euijoon, Hwang, Nong-Moon, Kim, Doh-Yeon, Ho, K.M.: Phys. Rev. Lett. **95**, 205501 (2005)
28. Lee, Gun-Do, Wang, C.Z., Yoon, Euijoon, Hwang, Nong-Moon, Ho, K.M.: Phys. Rev. B. **74**, 245411 (2006)
29. Lee, Gun-Do, Wang, C.Z., Yu, Jaejun, Yoon, Euijoon, Hwang, Nong-Moon, Ho, Kai-Ming: Phys. Rev. B **76**, 165413 (2007)
30. Lee, Gun-Do, Wang, C.Z., Yu, Jaejun, Yoon, Euijoon, Hwang, Nong-Moon, Ho, Kai-Ming: Appl. Phys. Lett. **92**, 043104 (2008)
31. Kaxiras, E., Pandey, K.C.: Phys. Rev. Lett. **61**, 2693 (1988)
32. Nordlund, K., Keinonen, J., Mattila, T.: Phys. Rev. Lett. **77**, 699 (1996)
33. Ewels, C.P., Telling, R.H., El-Barbary, A.A., Heggie, M.I., Briddon, P.R.: Phys. Rev. Lett. **91**, 025505 (2003)
34. Lu, A.J., Pan, B.C.: Phys. Rev. Lett. **92**, 105504 (2004)
35. Sammalkorpi, M., Krasheninnikov, A., Kuronen, A., Nordlund, K., Kaski, K.: Phys. Rev. B **70**, 245416 (2004)
36. Terrones, H., Terrones, M., Herna'ndez, E., Grobert, N., Charlier, J.-C., Ajayan, P.M.: Phys. Rev. Lett. **84**, 1716 (2000)
37. Hashimoto, A., Suenaga, K., Gloter, A., Urita, K., Iijima, S.: Nat. Lond. **430**, 870 (2004)
38. Yakobson, B.I.: Appl. Phys. Lett. **72**, 918 (1998)
39. Mori, H., Ogata, S., Li, S.J., Akita, S., Nakayama, Y.: Phys. Rev. B **76**, 165405 (2007)
40. Arakawa, K., Ono, K., Isshiki, M., Mimura, K., Uchikoshi, M., Mori, H.: Science **318**, 956 (2007)
41. Morris, J.R., Lu, Z.Y., Ring, D.M., Xiang, J.B., Ho, K.M., Wang, C.Z., Fu, C.L.: Phys. Rev. B **58**, 11241 (1998)
42. Kwon, I., Biswas, R., Wang, C.Z., Ho, K.M., Soukoulis, C.M.: Phys Rev B **49**, 7242 (1994)

43. Tersoff, J.: Phys. Rev. B **38**, 9902 (1988)
44. Lenosky, T.J., Sadigh, B., Alonso, E., Bulatov, V.V., Diaz de la Rubia, T., Kim, J., Voter, A.F., Kress, J.D.: Model. Simul. Mater. Sci. Eng. **8**, 825 (2000)
45. Lee, Gun-Do, Wang, C.Z., Lu, Z.Y., Ho, K.M.: Phys. Rev. Lett. **81**, 5872 (1998)
46. Lee, Gun-Do, Wang, C.Z., Lu, Z.Y., Ho, K.M.: Surf. Sci. **426**, L427 (1999)
47. Zhang, Z., Wu, F., Zandvliet, H.J.W., Poelsema, B., Metiu, H., Lagally, M.G.: Phys. Rev. Lett. **74**, 3644 (1995)
48. Swartzentruber, B.S., Smith, A.P., Jönsson, H.: Phys. Rev. Lett. **77**, 2518 (1996)
49. Dijkkamp, D., van Loenen, E.J., Elswijk, H.B.: In: Proceedings of the 3rd NEC Symposium on Fundamental Approach to New Material Phases, Springer Series on Material Science. Springer, Berlin (1992)
50. Bedrossian, P.J.: Phys. Rev. Lett. **74**, 3648 (1995)
51. Brocks, G., Kelly, P.J.: Phys. Rev. Lett. **76**, 2362 (1996)
52. Yamasaki, T., Uda, T., Terakura, K.: Phys. Rev. Lett. **76**, 2949 (1996)
53. Chadi, D.J.: Phys. Rev. Lett. **43**, 43 (1979)
54. Wolkow, R.A.: Phys. Rev. Lett. **68**, 2636 (1992)
55. Zhang, Z., Wu, F., Lagally, M.G.: Surf. Rev. Lett. **3**, 1449 (1996)
56. Swartzentruber, B.S.: Phys. Rev. Lett. **76**, 459 (1996)
57. Borovsky, B., Krueger, M., Ganz, E.: Phys. Rev. Lett. **78**, 4229 (1997)
58. Goringe, C.M., Bowler, D.R.: Phys. Rev. B **56**, R7073 (1997)
59. Rabier, J., Cordier, P., Demenet, J.L., Garem, H.: Mater. Sci. Eng. A **309**, 74 (2001)
60. Suzuki, T., Yasutomi, T., Tokuoka, T., Yonenaga, I.: Phys. Status Solidi A **171**, 47 (1999)
61. Koizumi, H., Kamimura, Y., Suzuki, T.: Philos. Mag. A **80**, 609 (2000)
62. Pizzagalli, L., Beauchamp, P.: Philos. Mag. Lett. **84**, 729 (2004)
63. Wang, C.Z., Li, Ju, Ho, K.M., Yip, S.: Appl. Phys. Lett. **89**, 051910 (2006)
64. Pirouz, P., Demenet, J.L., Hong, M.H.: Philos. Mag. A **81**, 1207 (2001)
65. Marder, M.P.: Condensed Matter Physics. 2nd edn. Wiley, New York (2000)
66. Lin, X., Li, J., Först, C.J., Yip, S.: Proc. Natl. Acad. Sci. USA **103**, 8943 (2006)
67. Haas, H., Wang, C.Z., Fahnle, M., Elsasser, C., Ho, K.M.: Phys. Rev. B **57**, 1461 (1998)
68. Haas, H., Wang, C.Z., Fahnle, M., Elsasser, C., Ho, K.M.: In: Turchi, P.E.A., et al. (eds.) MRS Symposium Proceedings, vol. 491, p. 327 (1998)
69. Haas, H., Wang, C.Z., Fahnle, M., Elsasser, C., Ho, K.M.: J. Phys. Condens. Matter **11**, 5455 (1999)
70. Haas, H., Wang, C.Z., Ho, K.M., Fahnle, M., Elsasser, C.: Surf. Sci. **457**, L397 (2000)
71. Li, Ju, Wang, C.Z., Chang, J.-P., Cai, W., Bulatov, V., Ho, K.M., Yip, S.: Phys. Rev. B **70**, 104113 (2004)
72. Chuang, Feng-chuan, Wang, C.Z., Ho, K.M.: Phys. Rev. B **73**, 125431 (2006)
73. Zhang, Wei, Lu, Wen-Cai, Sun, Jiao, Zhao, Li-Zhen, Wang, C.Z., Ho, K.M.: Chem. Phys. Lett. **455**, 232 (2008)
74. Lu, W.C., Wang, C.Z., Ho, K.M.: (to be published)
75. Tang, Mingsheng, Wang, C.Z., Lu, W.C., Ho, K.M.: Phys. Rev. B **74**, 195413 (2006)
76. Lu, W.C., Wang, C.Z., Schmidt, M.W., Bytautas, L., Ho, K.M., Ruedenberg, K.: J. Chem. Phys. **120**, 2629 (2004)
77. Lu, W.C., Wang, C.Z., Schmidt, M.W., Bytautas, L., Ho, K.M., Ruedenberg, K.: J. Chem. Phys. **120**, 2638 (2004)
78. Lu, W.C., Wang, C.Z., Chan, Z.L., Ruedenberg, K., Ho, K.M.: Phys. Rev. B (Rapid Commun.) **70**, 041101 (2004)
79. Lu, W.C., Wang, C.Z., Ruedenberg, K., Ho, K.M.: Phys. Rev. B **72**, 205123 (2005)
80. Chan, T.-L., Yao, Y.X., Wang, C.Z., Lu, W.C., Li, J., Qian, X.F., Yip, S., Ho, K.M.: Phys. Rev. B **76**, 205119 (2007)
81. Qian, X.-F., Li, J., Wang, C.-Z., Qi, L., Chan, T.-L., Yao, Y.-X., Ho, K.-M., Yip, S.: Phys. Rev. B (to be published)